

This is the author's final, peer-reviewed manuscript as accepted for publication (AAM). The version presented here may differ from the published version, or version of record, available through the publisher's website. This version does not track changes, errata, or withdrawals on the publisher's site.

# High count rate pulse shape discrimination algorithms for neutron scattering facilities

S. Richards, G. J. Sykora, M. P. Taggart

## Published version information

**Citation:** S Richards, G Sykora and M Taggart. 'High count rate pulse shape discrimination algorithms for neutron scattering facilities.' Nucl Instrum Meth A, vol. 989 (2021): 164946.

**DOI:** [10.1016/j.nima.2020.164946](https://doi.org/10.1016/j.nima.2020.164946)

©2020. This manuscript version is made available under the [CC-BY-NC-ND](https://creativecommons.org/licenses/by-nc-nd/4.0/) 4.0 Licence.

This version is made available in accordance with publisher policies. Please cite only the published version using the reference above. This is the citation assigned by the publisher at the time of issuing the AAM. Please check the publisher's website for any updates.

# High Count Rate Pulse Shape Discrimination Algorithms for Neutron Scattering Facilities

S. Richards<sup>1</sup>, G. J. Sykora<sup>2</sup>, M. P. Taggart<sup>3</sup>

[1] Detector Development Group – Science and Technology Facilities Council, Rutherford Appleton Laboratory, Harwell Science and Innovation Campus, Didcot, Oxfordshire, OX11 0QX. These authors contributed equally to this work. [2] ISIS Detector Group – Science and Technology Facilities Council, Rutherford Appleton Laboratory, Harwell Science and Innovation Campus, Didcot, Oxfordshire, OX11 0QX. [3] Department of Physics, University of Surrey, Guildford, Surrey, GU2 7XH

## Abstract

The performance of EJ-270, a <sup>6</sup>Li loaded pulse shape discriminating plastic scintillator was tested for use in applications with high thermal and epithermal neutron fluxes such as neutron scattering facilities. The short decay time of EJ-270 make it of interest for high count rate applications. To realize this, 4 PSD algorithms were tested. The algorithms were selected based on the potential for high rate applications and simplicity. These algorithms were the charge integration method with and without the addition of a digital low pass filter, a measurement of the time to 10% of peak amplitude and a method we call the “tail sum” which utilizes a digital low pass filter and sums a small number of samples in the tail of each pulse. These algorithms were benchmarked using the figure of merit, the  $\gamma$ -sensitivity and potential rate capability. The charge integration method gave the highest figure of merit of 1.37 using a long window of 272.5 ns but had a  $\gamma$ -sensitivity of  $2 \times 10^{-6}$  which was poorer than the tail sum algorithm. The tail sum algorithm was able to achieve a figure of merit of 1.36 with a window of 250 ns and a  $\gamma$ -sensitivity on the order of  $10^{-7}$ . Reducing the integration windows to match the fastest algorithm of time to 10% resulted in the tail sum outperforming the other algorithms with a figure of merit of 1.26 and a  $\gamma$ -sensitivity of  $6 \times 10^{-7}$ . The short charge integration method and tail-sum were compared on the EMMA beamline at the ISIS pulsed neutron and muon source. The tails sum demonstrated better separation between the  $\gamma$ -rays and thermal neutron at an incident peak neutron rate of  $9.6 \times 10^5$  neutrons per second.

Keywords: EJ-270, Scintillator, Neutron Scattering, Thermal Neutron Detection, Pulse Shape Discrimination.

## 1. Introduction

Spallation neutron sources are an important tool for material science. The use of thermal and epithermal neutrons from these sources enable techniques such as powder and single crystal diffraction, neutron reflectometry, small angle scattering and imaging. Next generation sources such as the European Spallation Source and upgrades to current facilities such as J-Parc, the Spallation Neutron Source, and the ISIS pulsed neutron and muon source will generate high neutron fluxes which pose challenges to current detector technologies [1]. The scintillation detectors ISIS currently utilises are cerium doped <sup>6</sup>Li-glass and ZnS:Ag/<sup>6</sup>LiF scintillators. However, the glass suffers from high  $\gamma$ -ray sensitivity and ZnS:Ag has a long afterglow which limits its applications at high rate [2]. The recently developed <sup>6</sup>Li-loaded plastic scintillator, EJ-270, is of interest owing to the fast decay, the inherent low  $\gamma$ -sensitivity, and pulse shape discrimination (PSD) properties.

40 The  $^6\text{Li}$  containing EJ-270 plastic scintillator, developed by Eljen Technologies and Lawrence  
41 Livermore National Laboratories, exhibit pulse shape discrimination of  $\gamma$ -ray and charged particle  
42 events [3, 4]. Typical of polyvinyl toluene (PVT) based scintillators, EJ-270 is low cost, available in  
43 large volumes and, despite fogging in certain environments, maintains good environmental stability  
44 [5]. These attributes make EJ-270 an attractive alternative to other fast PSD scintillators such as CLYC  
45 [6,7] particularly in applications where good energy resolution is not a requirement.

46 Pulse shape discriminating scintillators are popular for applications in homeland security where  
47 special nuclear materials such as  $^{235}\text{U}$ ,  $^{233}\text{U}$  and  $^{239}\text{Pu}$  emit neutrons during spontaneous fission  
48 events. Detectors capable of discriminating neutrons from  $\gamma$ -ray events allow for the neutrons  
49 emitted from these materials to be detected with high confidence. The research effort in this field  
50 has focussed on utilising PSD for detecting fast neutrons ( $E_k > 1\text{MeV}$ ) in plastic scintillators [8, 9, 10,  
51 11]. The key differences between the homeland security applications and neutron scattering are the  
52 energy and flux of the incident radiation. For neutron scattering only epithermal, thermal and cold  
53 neutrons are of interest. Sensitivity to these neutron energies is provided through the addition of  $^6\text{Li}$   
54 to the plastic base polymer. The neutron flux is significantly higher at a spallation neutron source  
55 than would be expected from an illicit sample of special nuclear materials leading to pulse pile up.  
56 Consequently, the fast decay time of EJ-270 makes it attractive for high rate applications such as  
57 single point detectors for reflectometry, small angle neutron scattering, or beamline diagnostics. A  
58 short decay PSD scintillator such as EJ-270 would be needed for these applications along with the  
59 ability to perform pulse shape discrimination at high rates in real time.

60 A popular PSD algorithm is the charge comparison algorithm (discussed in more detail in section 3)  
61 [12]. This algorithm integrates the pulse from the scintillator using short and long time windows, the  
62 ratio between the long and short window gives a PSD parameter (Eq. 3) which can be used to  
63 discriminate neutron events from  $\gamma$ -ray events [3, 4]. For EJ-270 coupled to a photomultiplier tube  
64 (PMT), the long window time reported in the literature is 500 ns [4]. The decay of EJ-270 is however  
65 much faster. The time to 10% from peak amplitude is  $\sim 50\text{-}70$  ns depending on the exciting particle  
66 type [3, 4]. Therefore, an alternative to the charge integration algorithm utilizing the fast decay time  
67 could allow for higher count rates. While there are PSD algorithms found in the literature that can  
68 operate on very short sample lengths, such as the simplified digital charge collection algorithm, they  
69 usually rely on functions that are resource intensive for an FPGA [13]. The two high rate PSD  
70 algorithms presented in this work are “time to 10%” – a measurement of the delay between the  
71 peak amplitude of the pulse and its decay to 10% of that value, and “tail sum” – an integral across a  
72 small number of samples in the tail of the pulse.

73 Additional challenges to neutron scattering applications are that detectors are typically  
74 multichannel, large area and the physical constraints of the experimental setup typically results in  
75 long cables between detector elements. To achieve this, an algorithm capable of real time  
76 discrimination at high rates would be needed. An algorithm that is simple to implement on a FPGA  
77 would not only allow for minimal processing time in the FPGA but would also allow for more  
78 channels per FPGA, reducing the cost of large multi-channel systems or the use of more affordable  
79 FPGAs for smaller single channel systems.

80

81

## 2. Materials and Method

82

83 Two sets of experiments were performed to characterize EJ-270 and the PSD algorithms. The first set  
84 was algorithm development and testing using sealed sources and the second was count rate tests at  
85 the EMMA beamline at the ISIS Pulsed Neutron and Muon source [14].

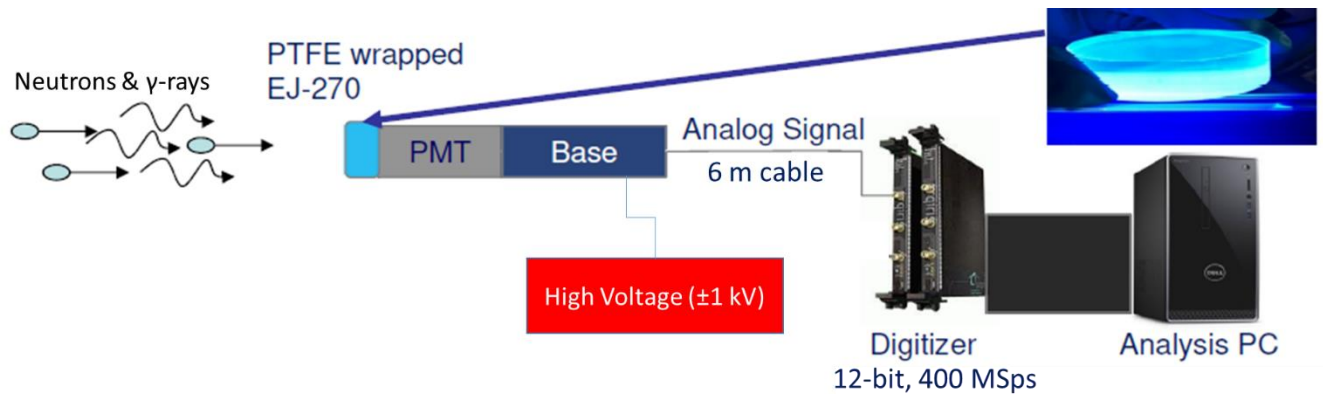
86

## 87 2.1 Detector configuration

88

89 The detector consisted of a 48 mm diameter x 15 mm thick cylinder of EJ-270 (shown in Fig. 1a)  
90 coupled to a Hamamatsu R6231-100 PMT using Dow Corning Vacuum grease. The scintillator was  
91 wrapped in PTFE tape to enhance light collection. The coupled EJ270/PMT system was encased in a  
92 light-tight aluminum enclosure. A negatively biased E1198-26 base at -1000 V was used to avoid  
93 signal reduction effects due to charge build up on the decoupling capacitor of positively biased bases  
94 such as those typically used with PSD plastic scintillators. A 6 m long coaxial cable was used from the  
95 PMT to the digitizer. Testing on the EMMA beamline (described below) required a 30 m long cable  
96 due to space restrictions on the beamline. Signals from the PMT were digitized using an Acqiris 400  
97 MSps 12-bit digitizer with trace lengths of 500 ns. Traces were stored for off-line processing using  
98 Python.

99



100

101 Figure 1. The schematic of the detector configuration.

## 102 2.2 Irradiation conditions

103

104 Pulse shape discrimination algorithms were tested using measurements from a water moderated  
105  $^{241}\text{Am}$ -Be source (370 GBq activity) shielded with lead. The detector was placed 50 cm from the  
106 source providing a uniform neutron flux of approximately 100 neutrons per second per  $\text{cm}^2$ . Gamma  
107 sensitivity was assessed by placing the detector 30 cm from a 7.4 MBq  $^{60}\text{Co}$  source.

108

109 The performance of EJ-270 as a function of neutron flux was tested on the EMMA beamline at the  
110 ISIS Pulsed Neutron and Muon source. EMMA has a direct line of site to the room temperature  
111 water moderator on ISIS. The instrument flight path is 15.6m long. Neutrons are in a range from  
112 approximately 500 meV (0.4 Å) to 3.25 meV (5 Å) with a peak energy of 80 meV (1 Å in wavelength).  
113 Higher energy neutrons are chopped out and further discriminated by time of flight. All  
114 measurements presented here were time gated to measure a neutron energy range of 75 meV – 90  
115 meV. The neutron flux on EMMA at 80 meV is  $1 \times 10^6$  neutrons per second per  $\text{cm}^2$ . The overall  
116 incident flux on the detector was controlled by a set of cadmium slits upstream of the detector.

117 There is a wide range of gamma energies from (n,  $\gamma$ ) reactions in beamline components. The  
118 prominent energy is the prompt emission of a 480 keV gamma from neutron capture by  $^{10}\text{B}$ .  
119

### 120 3. Signal Processing

121

122 Typical PSD algorithms utilize charge integration over two different length time windows as defined  
123 in eq. 1 and eq. 2. The two charges are then compared as in eq. 3 to yield a value for pulse shape.  
124 Figure 2 depicts a representative signal with the windows shown for illustrative purposes.

$$125 \quad Q_s = \int_{t_0}^{t_{short}} y(t) dt \quad (1)$$

$$126 \quad Q_l = \int_{t_0}^{t_{long}} y(t) dt \quad (2)$$

$$127 \quad PSD_Q = 1 - \frac{Q_s}{Q_L} \quad (3)$$

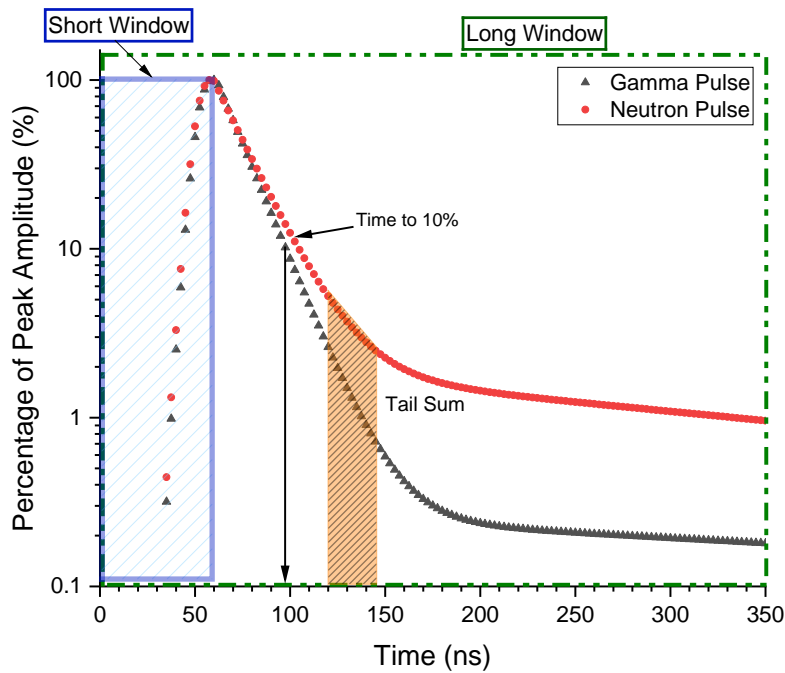
128 Two alternative PSD methods investigated here are a time to 10% of the pulse height and integrating  
129 charge in only a short window in the tail of the signal (referred to as the tail sum). Both methods are  
130 also represented in figure 2. All three methods are compared here.

131 The time to 10% algorithm is conceptually the simplest of the three tested algorithms. A neutron  
132 event has a longer decay and therefore discrimination can be identified by its longer time to 10%.  
133 This specific percentage was selected based on study of the pulse shapes and basic optimisation, a  
134 different percentage could be used with other scintillators.

135 The tail sum algorithm consists of summing the amplitude,  $V_{st}$ , from the digitizer over a set number  
136 of samples,  $i$ , (analogous to window length) starting a time,  $t_{D1}$ , after the peak. Then this sum is  
137 normalized to the peak amplitude of the pulse (explained below),  $V_p$ , allowing for the increase in tail  
138 sum with pulse height to be accounted for (Eq. 4).

$$139 \quad PSD_{TS} = \frac{1}{V_p} \sum_{st=T_{D1}}^{T_{D1+i}} V_{st} \quad (4)$$

140



141

142 Figure 2. The schematic of typical pulses from a pulse shape discriminating scintillator showing how  
 143  $\gamma$ -rays and neutrons differ and showing the three PSD algorithms. The window position are  
 144 representative and do not show the exact window length and position of each algorithm.

145 The digitized pulses were processed using Python. For the sealed source data each trace contained  
 146 only one pulse allowing the numpy max function to accurately report the peak amplitude [15]. The  
 147 traces from the EMMA instrument contained multiple pulses and therefore the peak finding function  
 148 in the peakutils library was used. The pulse shape discrimination was performed using the time to  
 149 10% algorithm, the tail sum algorithm and the charge integration algorithm with and without a  
 150 digital low pass filter. The filter from the scipy library was a first order digital low pass Bessel filter  
 151 with a 10 MHz cut off frequency, it was used with the tail sum and time to 10% algorithms [16]. The  
 152 charge integration algorithm was tested with and without the low pass Bessel filter. No other  
 153 processing such as baseline correction was applied to the data. While a DC offset was present no  
 154 shift in the offset was observed. As we were focused on the thermal neutron peak the lack of offset  
 155 removal did not influence the charge integration algorithm results. A basic energy calibration was  
 156 performed based on the Compton edges from the 1.17 and 1.33 MeV  $^{60}\text{Co}$  gamma rays and the 480  
 157 keV gamma ray emitted by the  $^{10}\text{B}$  neutron capture reaction.

158 The most common method for quantifying the performance of a PSD based detector is the Figure of  
 159 Merit (FoM) [17]. The FoM (Eq. 5) is determined for a given energy range by plotting the distribution  
 160 of the pulse shape parameter and calculating the separation of the peaks and their full widths at half  
 161 maximum.

162 
$$FoM = \frac{Centroid_n - Centroid_\gamma}{FWHM_n + FWHM_\gamma} \quad (5)$$

163 Typically the FoM will be calculated from data acquired on a sealed source such as an Americium-  
 164 Beryllium or Californium sources, both of which can be moderated to produce thermal neutrons.  
 165 While this method of quantification works well for homeland security, it has limitations for neutron

166 scattering instrumentation. The  $\gamma$ -ray background at a neutron scattering experiment changes with  
167 the experimental setup. Different samples produce different backgrounds, the use of boron,  
168 cadmium or gadolinium based shielding and beam jaws also change the background, as such the  $\gamma$ -  
169 ray sensitivity is a preferred measure of discrimination.

170 The  $\gamma$ -ray sensitivity measurement is performed using a prolonged measurement on a pure  $\gamma$ -ray  
171 source such as  $^{60}\text{Co}$ . After background subtraction, the ratio between the number of incident  $\gamma$ -rays  
172 and the number of events that the system identifies as neutrons gives the  $\gamma$ -ray sensitivity [18,19].  
173 This is effectively a false positive rate.

174 An optimization script iterated the start and end points of the integration windows for both forms of  
175 the charge integration and the single window for the tail sum. The script measured the gamma  
176 sensitivity and the figure of merit for the energy range corresponding to  $\pm 2$  standard deviations ( $\sigma$ )  
177 from the centroid of the neutron capture peak for each possible window combination. The  
178 optimization of time to 10% was basic and not as exhaustive as the other optimizations. The script  
179 measured the figure of merit and gamma sensitivity using the same methodology as the other  
180 algorithms but the tested values ranged from time to 15% to time to 5% in steps of 1%.

181 The optimization for count rate limited the maximum value of the window to match the duration of  
182 the time to 10% algorithm.

183 The performance of the algorithms were evaluated by comparing the FoM, the sensitivity to  $^{60}\text{Co}$   $\gamma$ -  
184 ray in the region corresponding to the  $^6\text{Li}$  neutron capture peak, and the duration of the  
185 measurement to achieve discrimination.

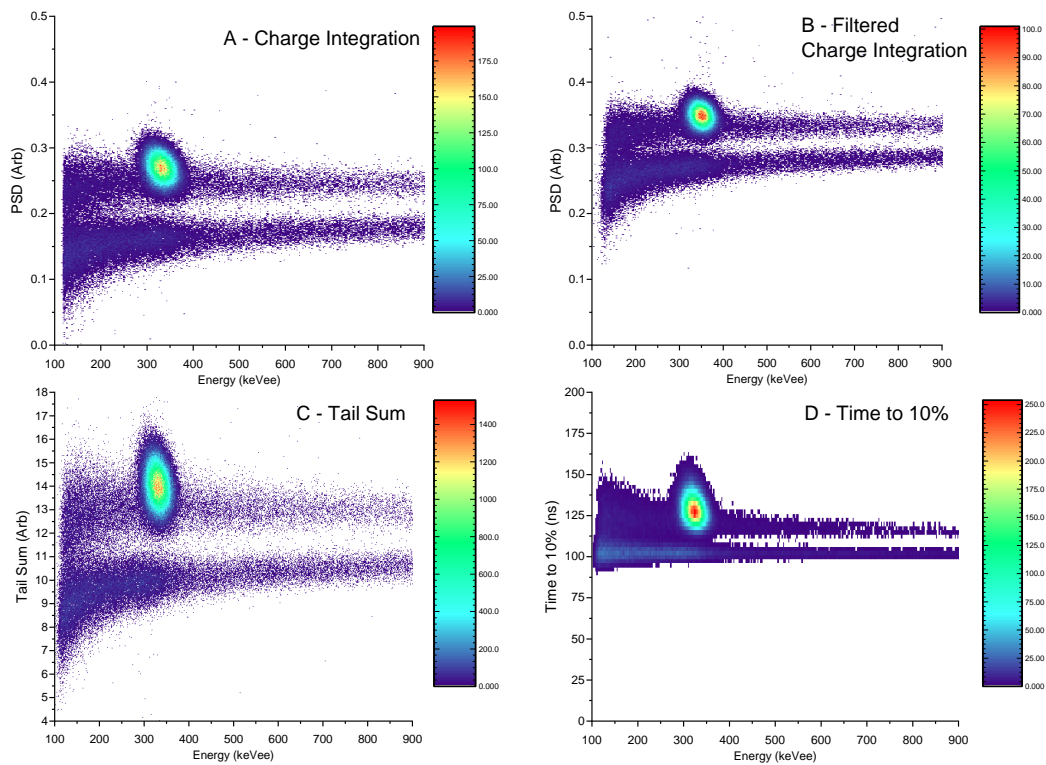
## 186 **4. Results and Discussion**

187

### 188 **4.1 Optimizing processing parameters – Sealed Source Results**

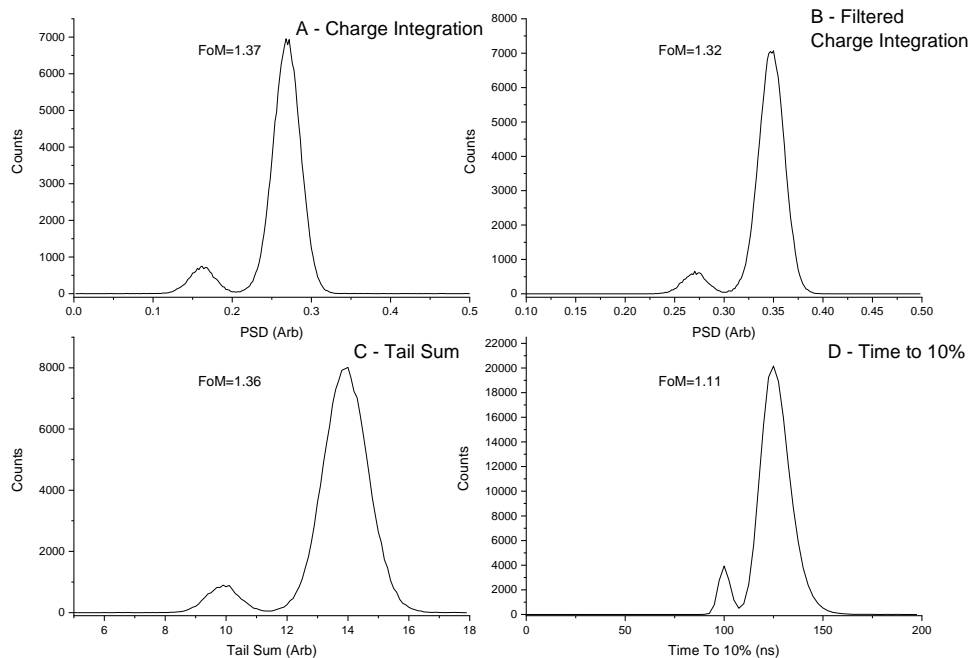
189

190 2D histograms of gamma equivalent energy vs. PSD parameter for each tested algorithm from data  
191 taken on the moderated  $^{241}\text{Am}$ -Be source are shown in figure 3. The figures show the characteristic  
192 thermal neutron capture peak at  $\sim 300$ -400 keVee which overlays the continuum of fast neutrons, at  
193 a lower PSD value, the continuum from  $\gamma$ -rays is observed. All 4 algorithms show some separation  
194 between the  $\gamma$ -rays and the thermal neutron peak. This separation is better demonstrated in figure  
195 4, which shows the distribution of the PSD parameter for each tested algorithm, at the energy range  
196 corresponding to thermal neutron events. The figure of merit is calculated using equation 5 after  
197 fitting each distribution using a double Gaussian function. For both figures the sub-figures labelled  
198 "A" are the standard charge integration method, "B" corresponds the charge integration algorithm  
199 but after applying a digital low pass filter to the traces, "C" shows the tail sum results and D is the  
200 time to 10%.



201  
202  
203

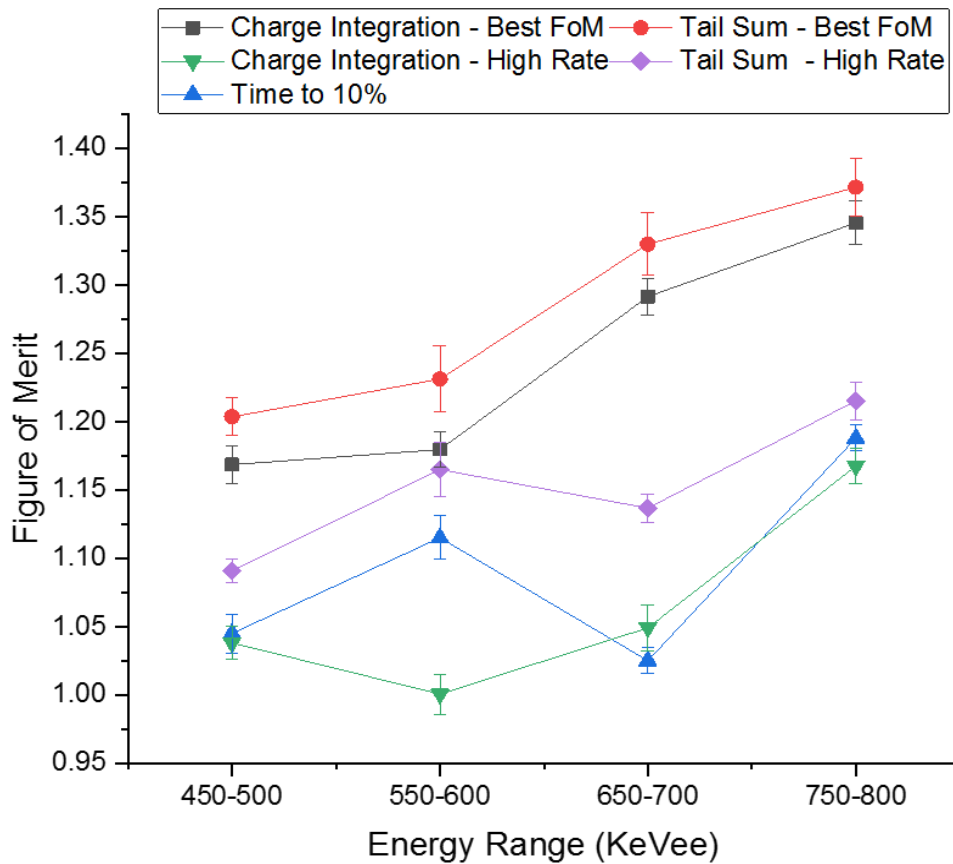
Figure 3. 2D PSD histograms for A: charge integration, B: Filtered Charge integration, C: Tail sum, D: Time to 10%.



204  
205  
206  
207

Figure 4. Histograms of counts as a function of PSD parameter for an energy range corresponding to the thermal neutron peak (270 keVee to 350 keVee) and their associated figure of merit for- A: charge integration, B: Filtered Charge integration, C: Tail sum and D: Time to 10%.

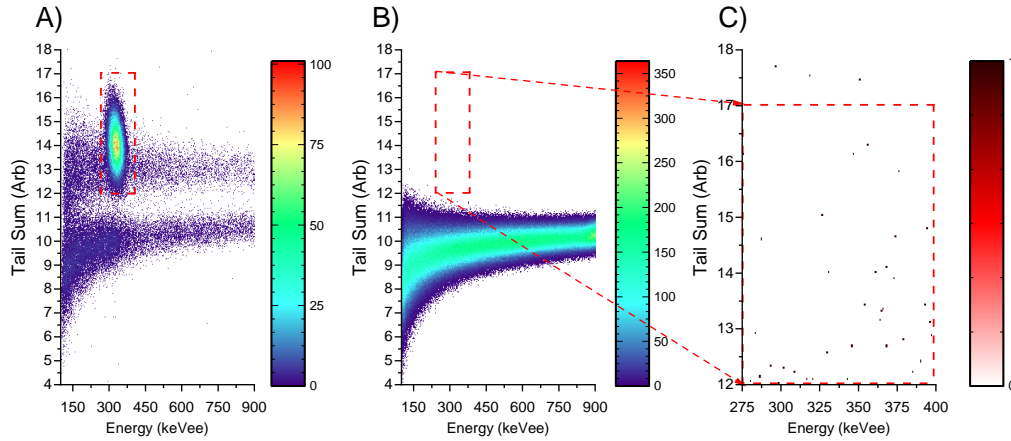
208 While fast neutrons are not the focus of this study, figures of merit for the best performing settings  
 209 of each different algorithms were plotted for 4 energy ranges as shown in figure 5. The Tail Sum  
 210 algorithm achieved the highest figure of merit. Figure of merit is seen to increase in general as the  
 211 energy increases for all PSD algorithms. Higher energy recoil protons and gammas result in overall  
 212 brighter events and better photon statistics accounting for improved figure of merit at higher  
 213 energies. A few exceptions occur around the 650-700 keVee range where the high rate algorithms  
 214 reduce slightly before increasing again. The exact cause of the reduced figure of merit is not yet  
 215 known, however the effect is minor and should not drastically affect overall performance.



216

217 Figure 5. The figure of merit as a function of electron equivalent energy for fast neutrons present in  
 218 the <sup>241</sup>Am-Be measurements for each tested algorithm.

219 The  $\gamma$ -sensitivity of the EJ-270 was measured using a moderated <sup>241</sup>Am-Be source and a <sup>60</sup>Co source.  
 220 The location of the neutron capture peak in terms of PSD and pulse height was determined using the  
 221 moderated <sup>241</sup>Am-Be source. A  $\pm 2\sigma$  boundary around the centroid of the neutron peak's pulse  
 222 height was used and a  $+2\sigma$  and  $-1.6\sigma$  boundary around the centroid of the neutron peak's PSD value.  
 223 These boundaries were then applied to <sup>60</sup>Co results along with a background subtraction, resulting in  
 224 the  $\gamma$  sensitivity factor (Figure 6).



225

226 Figure 6. 2D histograms showing PSD from A) a moderated  $^{241}\text{Am}$ -Be source B) plot from a  $^{60}\text{Co}$   
 227 source, and C) a zoom in of the region where thermal neutrons would appear. The features in A) are  
 228 thermal neutrons (highlighted by the box) and two horizontal bands; the lower band are  $\gamma$ -ray events  
 229 as they have faster decays and the upper band are fast neutron events.

230 The differences in the separation of the  $^6\text{Li}$  capture peak and the  $\gamma$ -ray background are evident in all  
 231 four plots. The addition of the low pass filter to the charge integration method resulted in a factor of  
 232 2.5 worse gamma sensitivity and reduction of 4% in figure of merit. The charge integration method  
 233 resulted in the best figure of merit of 1.37 but also a 22.5 ns longer measurement duration. Despite  
 234 the marginally lower figure of merit than the charge integration method, the tail sum method  
 235 resulted in the best  $\gamma$ -sensitivity of approximately  $10^{-7}$  counts per gamma. The time to 10% method  
 236 resulted in good  $\gamma$ -sensitivity but the worst figure of merit. Reducing the measurement duration to  
 237 match the fastest algorithm, time to 10%, resulted in the tail sum method having the best figure of  
 238 merit and the best  $\gamma$ -sensitivity of approximately  $6 \times 10^{-7}$  counts per gamma. It should be noted that  
 239 the accuracy of the  $\gamma$ -sensitivity results for the best tail sum measurement is limited by the counting  
 240 statistics of the number of  $\gamma$ -rays.

241 It is also worth noting that for similar figure of merit, the tail sum algorithm had a lower  $\gamma$ -sensitivity  
 242 than the charge integration method. Given that the figure of merit is a measure of the overlap in the  
 243 statistical distribution of both types of radiation, the same figure of merit should result in the same  
 244  $\gamma$ -sensitivity. A possible explanation in this discrepancy is that the assumption that data can be  
 245 described by a Gaussian is incorrect. Prusachenko *et al.* state that the assumption that the  
 246 distributions are Gaussian can only be made where there are no singularities from one region to  
 247 another [13]. Noise in the system, events such as direct hits to the PMT and pileup also appear as  
 248 events in the PSD and FoM plots which would create singularities from one region to another.

249 Table 1: Summary of performance for each algorithm with settings optimized for the best figure of  
 250 merit and settings corresponding to duration of the time to 10% algorithm.

Algorithm	Optimization	Figure of Merit	$\gamma$ -sensitivity ( $10^{-6}$ counts per gamma)	Duration* (ns)	Theoretical Count Rate (counts per second)
-----------	--------------	-----------------	--	-------------------	---

Charge integration	Figure of Merit	$1.37 \pm 0.008$	$2.0 \pm 0.66$	272.5	$3.67 \times 10^6$
Filtered Charge integration	Figure of Merit	$1.32 \pm 0.012$	$5.0 \pm 1$	267.5	$3.74 \times 10^6$
Tail sum	Figure of Merit	$1.36 \pm 0.014$	$\leq 0.1 \pm 0.59$	250	$4.00 \times 10^6$
Charge integration	Count Rate	$1.21 \pm 0.004$	$7.0 \pm 1.1$	125	$8 \times 10^6$
Filtered Charge integration	Count Rate	$1.21 \pm 0.004$	$7.0 \pm 1.0$	125	$8 \times 10^6$
Tail sum	Count Rate	$1.26 \pm 0.009$	$0.6 \pm 0.69$	125	$8 \times 10^6$
Time to 10%	N/A	$1.11 \pm 0.035$	$3.0 \pm 0.86$	$125 \pm 14$	$8 \times 10^6$

251 \* Errors on the duration for all algorithms apart from time to 10% is  $\pm 2.5$  ns which is the length of  
252 one sample.

253 A summary of the performance of each algorithm is displayed in table 1. Results are displayed for  
254 the optimization for best figure of merit and for duration that matched the time to 10% in count  
255 rate. The best gamma sensitivity of approximately  $10^{-7}$  is achieved with the tail sum method  
256 optimized for rejecting gammas. The high rate optimization was taken to be the same measurement  
257 duration corresponding to the average time to 10% for the neutron pulses. Table 1 includes a  
258 simplified measure indicative of the upper limit of count rate capability. The theoretical count rate  
259 shown can only be achieved given a regular, repetitive pulse whereas the signals of interest are  
260 much more random. The actual count rate achievable with each algorithm can be up to a factor of  
261 10 smaller and will be investigated in the future.

## 262 4.2 Performance at high incident neutron rates

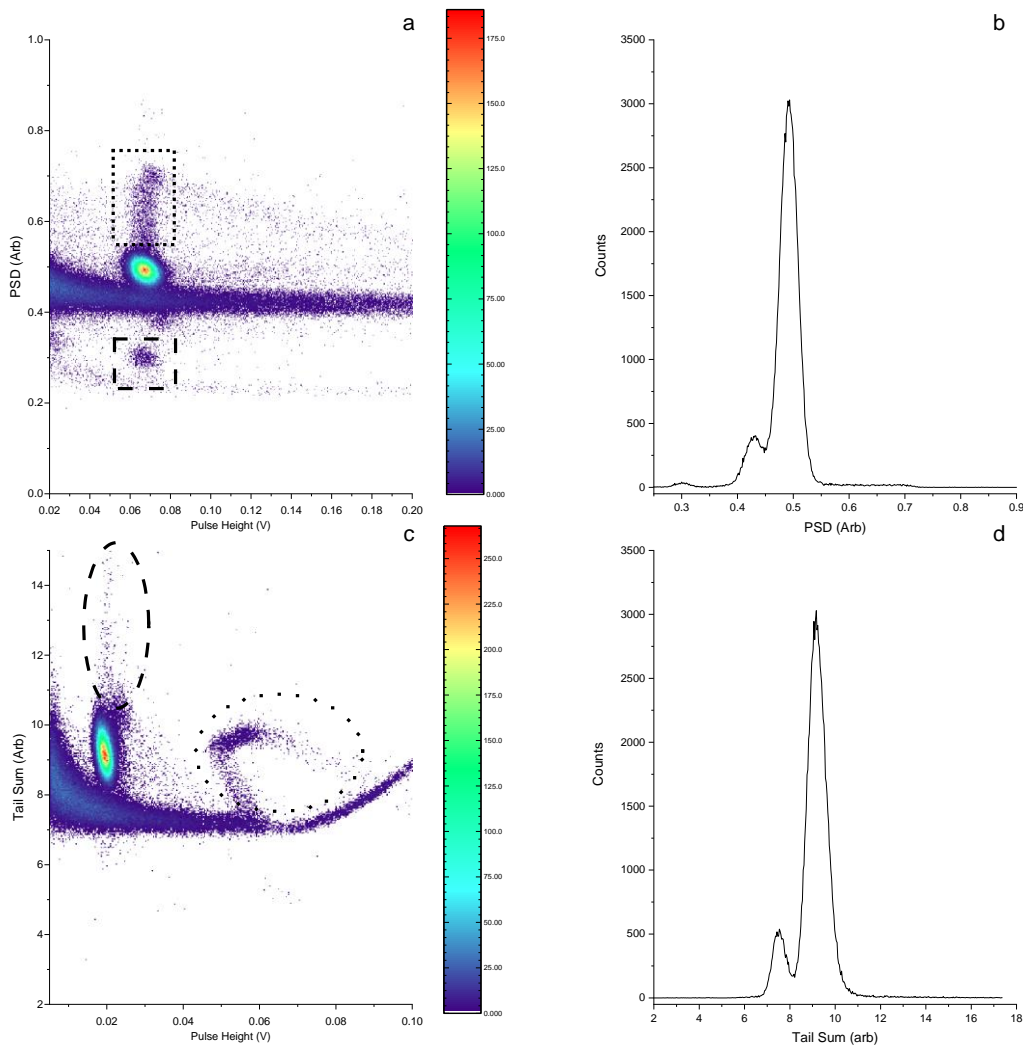
263 The 2D pulse shape histograms of data taken at a peak neutron rate of 960 knps using the charge  
264 integration method and the tail sum methods are shown in figure 7c and 7d respectively. The tail  
265 sum method was used over the time to 10% due to its compromise between superior gamma  
266 sensitivity and short duration as discussed in section 4.1. Here it is obvious that the thermal neutron  
267 peak is better separated from the gamma when using the tail sum method. No fast neutrons are  
268 visible because they are rejected by time of flight on the EMMA beamline.

269 Several interesting artefacts related to pulse pile-up can be seen in figure 7 that are not present in  
270 the PSD plots for the data taken on the  $^{241}\text{Am}$ -Be source (figure 3). There are four possibilities of  
271 pileup on the EMMA beamline: neutron-neutron, gamma-gamma, neutron-gamma and gamma-  
272 neutron. The neutron-neutron pileup events are most probable at high incident neutron rates while  
273 the gamma-gamma events are probable at low incident neutron rates due to  $(n, \gamma)$  reactions in the  
274 shielding.

275 Pileup artefacts manifest in different ways for the two PSD algorithms depending on the arrival time  
276 of the second event with respect to the first. In the charge integration method, if the second pulse  
277 arrives within the short window, then the PSD is reduced leading to the regions observed below the  
278 standard gamma continuum in figure 7a due to pulse height being determined by the type of

279 radiation arriving first. If, for example, a neutron arrives followed by a gamma within the short  
 280 window, then the pulse height is measured to be that of the neutron but the PSD value is  
 281 significantly reduced because of the large  $Q_s$  leading to the small island region highlighted by the  
 282 black dashed line box located around 0.07 V and 0.3 a.u. for the PSD value. If the arrival time of the  
 283 second event is outside the short window but within the long window, the PSD value of the charge  
 284 integration will increase thus leading to the extra events observed above the gamma continuum and  
 285 outside the thermal neutron peak. Again, the type of the initial radiation determines the pulse  
 286 height. Therefore, the line of events extending vertically from the thermal neutron peak in figure 7a,  
 287 highlighted by the black dotted square all contain at least one neutron. Likewise, any event outside  
 288 of the thermal neutron pulse height window contains at least one gamma event. The type of the  
 289 second interaction is, however, entirely ambiguous using these methods. The probability of a second  
 290 event occurring outside the short window and within the long window is significantly higher than  
 291 two events occurring within the short window accounting for the larger number of events above the  
 292 gamma continuum.

293



294

295 Figure 7: PSD Plots for the for the (a) charge integration and (c) tail sum algorithms optimized for  
296 count rate along with corresponding cuts across the PSD axis for the energy corresponding to  
297 thermal neutrons shown in (b) for charge integration and (c) for tail sum at peak incident rate 960  
298 knps at the EMMA beamline at ISIS.

299 Pileup artefacts for the tail sum method will only result in larger PSD values owing to integrating in  
300 only a single short window. This short duration of integration also means that the number of pileup  
301 events is significantly reduced over the charge integration method. Because the re-trigger time of  
302 the tail sum method is shorter, events that would have occurred within the long window are  
303 counted as separate events. These will, however, suffer from baseline issues. The pulse height of  
304 these events will be larger compared to those that are well separated in time because the event  
305 occurs on the tail of the scintillator emission. The thermal neutron peak is therefore broadened in  
306 pulse height as seen in figure 7c. If the second event occurs within the tail sum integration time,  
307 then the PSD value will increase (eq 4) giving rise to the vertical line of events extending from the  
308 thermal neutron peak, highlighted by the black dotted ellipse, and also the slight reduction of FoM  
309 illustrated in figure 7d. Events with pulse height greater than 0.04 V in figure 7c are a result of the  
310 pulses clipping on the ADC and subsequent smearing of the signal by the Bessel filter. In this case,  
311 the tail sum increases rapidly while there is little change in the filtered pulse height. Clipped pulses  
312 with pileup are manifested in the region with pulse height greater than 0.04 V and tail sum value  
313 above the standard gamma continuum, as highlighted by the black dotted circle. The slope and  
314 position of those features are dependent on the sample at which the tail sum starts and the number  
315 of samples integrated over. Further investigations on the tail sum algorithm performance at high  
316 rate will be carried out and reported on in subsequent papers.

317

## 5. Conclusion

318 The new  ${}^6\text{Li}$  loaded plastic scintillator EJ-270 has clear potential for high count rate applications  
319 when coupled with a negative polarity PMT base. The performance of EJ-270 was investigated along  
320 with four different pulse shape discrimination algorithms. The tail sum method was found to give the  
321 best results when the measurement duration of the algorithms were set to match the time to 10%.  
322 The figure of merit for this duration of 125 ns was 1.26 and the  $\gamma$ -sensitivity was  $6 \times 10^{-7}$ . The addition  
323 of a digital low pass filter to the charge integration method was found to reduce the best achievable  
324 figure of merit and  $\gamma$ -sensitivity but resulted in a slight increase in figure of merit for the short  
325 duration measurements.

326 The tail sum algorithm developed here to exploit the high count rate potential of EJ-270 is  
327 mathematically simple, and can be easily implemented into an FPGA for real time high rate  
328 applications. The tail sum algorithm outperformed the traditional charge integration algorithm in  
329 terms of  $\gamma$  sensitivity, and ultimate rate capability. The charge integration method had the best  
330 figure of merit when a long duration sample window was used. However, when pushing the limits of  
331 the algorithms in terms of short measurement windows the tail sum method was found to give the  
332 best figure of merit and  $\gamma$ -sensitivity. The implementation of the tail sum algorithm an FPGA will be  
333 the subject of a subsequent publication.

334

## Acknowledgements

335 This work was funded by the Science and Technology Facilities Council (STFC) through the ISIS  
336 department and the Centre for Instrumentation (CFI). We would also like to thank Matt Wilson and  
337 Paul Sellar of the STFC's Technology Department's Detector Development Group, Nigel Rhodes and  
338 Erik Schooneveld of STFC's ISIS Neutron Detector Group and Paul Sellin at the University of Surrey  
339 for supporting this work. We would also like to thank the author of the PeakUtils python library.

340

341

## References

342 [1] I. Stefanescu, M. Christensen, J. Fenske, R. Hall-Wilton, P.F. Henry, O. Kirstein, M. Müller, G.  
343 Nowak, D. Pooley, D. Raspino, N. Rhodes, J. Šaroun, J. Schefer, E. Schooneveld, J. Sykora, W.  
344 Schweika, Neutron detectors for the ESS diffractometers, *J. Inst.* 12 (2017) P01019–P01019.  
345 <https://doi.org/10.1088/1748-0221/12/01/P01019>.

346

347 [2] N.J. Rhodes, E.M. Schooneveld, R.S. Eccleston, Current status and future directions of position  
348 sensitive neutron detectors at ISIS, *Nuclear Instruments and Methods in Physics Research Section A:  
349 Accelerators, Spectrometers, Detectors and Associated Equipment.* 529 (2004) 243–248.  
350 <https://doi.org/10.1016/j.nima.2004.04.152>.

351 [3] N. Zaitseva, A. Glenn, H. Paul Martinez, L. Carman, I. Pawełczak, M. Faust, S. Payne, Pulse shape  
352 discrimination with lithium-containing organic scintillators, *Nuclear Instruments and Methods in  
353 Physics Research Section A: Accelerators, Spectrometers, Detectors and Associated Equipment.* 729  
354 (2013) 747–754. <https://doi.org/10.1016/j.nima.2013.08.048>.

355 [4] N.J. Cherepy, R.D. Sanner, P.R. Beck, E.L. Swanberg, T.M. Tillotson, S.A. Payne, C.R. Hurlbut,  
356 Bismuth- and lithium-loaded plastic scintillators for gamma and neutron detection, *Nucl.  
357 Instruments Methods Phys. Res. Sect. A Accel. Spectrometers, Detect. Assoc. Equip.* 778 (2015) 126–  
358 132. <https://doi.org/10.1016/j.nima.2015.01.008>.

359

360 [5] M. Loyd, M. Pianassola, C. Hurlbut, K. Shipp, L. Sideropoulos, K. Weston, M. Koschan, C.L.  
361 Melcher, M. Zhuravleva, Effects of temporary fogging and defogging in plastic scintillators, *Nucl.  
362 Instruments Methods Phys. Res. Sect. A Accel. Spectrometers, Detect. Assoc. Equip.* 922 (2019) 202–  
363 208. <https://doi.org/10.1016/j.nima.2018.12.087>.

364

365 [6] S. Richards, G.J. Sykora, X-ray induced radiation damage in CLYC(Ce), *Nucl. Instruments Methods  
366 Phys. Res. Sect. A Accel. Spectrometers, Detect. Assoc. Equip.* 902 (2018) 45–50.  
367 <https://doi.org/10.1016/j.nima.2018.06.045>.

368

369 [7] J. Glodo, R. Hawrami, K.S. Shah, Development of Cs<sub>2</sub>LiYCl<sub>6</sub> scintillator, *J. Cryst. Growth.* 379  
370 (2013) 73–78. <https://doi.org/10.1016/j.jcrysgro.2013.03.023>.

371

372 [8] N. Zaitseva, B.L. Rupert, I. Pawełczak, A. Glenn, H.P. Martinez, L. Carman, M. Faust, N. Cherepy, S.  
373 Payne, Plastic scintillators with efficient neutron/gamma pulse shape discrimination, *Nucl.  
374 Instruments Methods Phys. Res. Sect. A Accel. Spectrometers, Detect. Assoc. Equip.* 668 (2012) 88–  
375 93. <https://doi.org/10.1016/j.nima.2011.11.071>.

376

377 [9] M. Flaska, S.A. Pozzi, Identification of shielded neutron sources with the liquid scintillator BC-  
378 501A using a digital pulse shape discrimination method, Nucl. Instruments Methods Phys. Res. Sect.  
379 A Accel. Spectrometers, Detect. Assoc. Equip. 577 (2007) 654–663.  
380 <https://doi.org/10.1016/j.nima.2007.04.141>.  
381

382 [10] S.D. Clarke, M. Flaska, S.A. Pozzi, P. Peerani, Neutron and gamma-ray cross-correlation  
383 measurements of plutonium oxide powder, Nucl. Instruments Methods Phys. Res. Sect. A Accel.  
384 Spectrometers, Detect. Assoc. Equip. 604 (2009) 618–623.  
385 <https://doi.org/10.1016/j.nima.2009.02.045>.  
386

387 [11] S.A. Pozzi, S.D. Clarke, M. Flaska, P. Peerani, Pulse-height distributions of neutron and gamma  
388 rays from plutonium-oxide samples, Nucl. Instruments Methods Phys. Res. Sect. A Accel.  
389 Spectrometers, Detect. Assoc. Equip. 608 (2009) 310–315.  
390 <https://doi.org/10.1016/j.nima.2009.07.007>.  
391

392 [12] G.F. Knoll, Radiation Detection and Measurement, 4th ed., John Wiley and Sons, 2010.  
393

394 [13] P.S. Prusachenko, V.A. Khryachkov, V. V. Ketlerov, M. V. Bokhovko, I.P. Bondarenko,  
395 Optimization of the n/γ separation algorithm for a digital neutron spectrometer, Nucl. Instruments  
396 Methods Phys. Res. Sect. A Accel. Spectrometers, Detect. Assoc. Equip. 905 (2018) 160–170.  
397 <https://doi.org/10.1016/j.nima.2018.07.062>.  
398

399 [14] G. J. Sykora, EMMA operating modes, STFC internal report (2015).  
400

401 [15] S. Van Der Walt, S.C. Colbert, G. Varoquaux, The NumPy array: A structure for efficient  
402 numerical computation, Comput. Sci. Eng. 13 (2011) 22–30. <https://doi.org/10.1109/MCSE.2011.37>.  
403

404 [16] P. Virtanen, R. Gommers, T.E. Oliphant, M. Haberland, T. Reddy, D. Cournapeau, E. Burovski, P.  
405 Peterson, W. Weckesser, J. Bright, S.J. van der Walt, M. Brett, J. Wilson, K.J. Millman, N. Mayorov,  
406 A.R.J. Nelson, E. Jones, R. Kern, E. Larson, C.J. Carey, Í. Polat, Y. Feng, E.W. Moore, J. VanderPlas, D.  
407 Laxalde, J. Perktold, R. Cimrman, I. Henriksen, E.A. Quintero, C.R. Harris, A.M. Archibald, A.H. Ribeiro,  
408 F. Pedregosa, P. van Mulbregt, A. Vijaykumar, A. Pietro Bardelli, A. Rothberg, A. Hilboll, A. Kloeckner,  
409 A. Scopatz, A. Lee, A. Rokem, C.N. Woods, C. Fulton, C. Masson, C. Häggström, C. Fitzgerald, D.A.  
410 Nicholson, D.R. Hagen, D. V. Pasechnik, E. Olivetti, E. Martin, E. Wieser, F. Silva, F. Lenders, F.  
411 Wilhelm, G. Young, G.A. Price, G.L. Ingold, G.E. Allen, G.R. Lee, H. Audren, I. Probst, J.P. Dietrich, J.  
412 Silterra, J.T. Webber, J. Slavič, J. Nothman, J. Buchner, J. Kulick, J.L. Schönberger, J.V. de Miranda  
413 Cardoso, J. Reimer, J. Harrington, J.L.C. Rodríguez, J. Nunez-Iglesias, J. Kuczynski, K. Tritz, M. Thoma,  
414 M. Newville, M. Kümmerer, M. Bolingbroke, M. Tartre, M. Pak, N.J. Smith, N. Nowaczyk, N.  
415 Shebanov, O. Pavlyk, P.A. Brodtkorb, P. Lee, R.T. McGibbon, R. Feldbauer, S. Lewis, S. Tygier, S.  
416 Sievert, S. Vigna, S. Peterson, S. More, T. Pudlik, T. Oshima, T.J. Pingel, T.P. Robitaille, T. Spura, T.R.  
417 Jones, T. Cera, T. Leslie, T. Zito, T. Krauss, U. Upadhyay, Y.O. Halchenko, Y. Vázquez-Baeza, SciPy 1.0:  
418 fundamental algorithms for scientific computing in Python, Nat. Methods. 17 (2020) 261–272.  
419 <https://doi.org/10.1038/s41592-019-0686-2>.  
420

- 421 [17] R.A. Winyard, J.E. Lutkin, G.W. McBeth, Pulse shape discrimination in inorganic and organic  
422 scintillators. I, Nucl. Instruments Methods. 95 (1971) 141–153. [https://doi.org/10.1016/0029-](https://doi.org/10.1016/0029-554X(71)90054-1)  
423 [554X\(71\)90054-1](https://doi.org/10.1016/0029-554X(71)90054-1).  
424
- 425 [18] R. Kouzes, J.R. Ely, A.T. Lintereur, D.L. Stephens. Neutron Detector Gamma Insensitivity Criteria.  
426 Pacific Northwest National Laboratory report PNNL-18903. (2009)  
427
- 428 [19] A. Khaplanov, F. Piscitelli, J.C. Clergeau, J. Correa, P. van Esch, M. Ferraton, R. Guerard and R.  
429 Hall-Wilton. Investigation of gamma-ray sensitivity of neutron detectors on thin converter films.  
430 Journal of Instrumentation, 8. (2013)  
431